A Compact, Low-Field, Broadband Matching Section for Externally Powered *X*-Band Dielectric-Loaded Accelerating Structures

Yelong Wei, Alexej Grudiev, Ben Freemire, and Chunguang Jing

***Abstract*— It has been technically challenging to efficiently couple external radio frequency (RF) power to cylindrical dielectric-loaded accelerating (DLA) structures, especially when the DLA structure has a high dielectric constant. This article presents a novel design of matching section for coupling the RF power from a circular waveguide to an *X*-band DLA structure with a dielectric constant $\varepsilon_r = 16.66$ and a loss tangent $\tan\delta = 3.43 \times 10^{-5}$. It consists of a compact dielectric disk with a width of 2.035 mm and a base angle of 60°, resulting in a broadband coupling at a low RF field, which has the potential to survive in the high-power environment. To prevent a sharp dielectric corner break, a 45° chamfer is also added. A microscale vacuum gap, caused by metallic clamping between the thin coating and the outer thick copper jacket, is also studied in detail. Through optimization, most of RF power is coupled into the DLA structure, with no enhancement of peak electromagnetic fields above those of the structure itself. Tolerance studies on the geometrical parameters and mechanical design of the full-assembly structure are also carried out as a reference for fabrication.**

***Index Terms*— Dielectric-loaded accelerating (DLA) structures, high accelerating gradient, linear accelerators, matching section, traveling wave.**

I. Introduction

DIELECTRIC-LOADED accelerating (DLA) structures, utilizing dielectrics to slow down the phase velocity of traveling waves in the vacuum channel, have been studied both theoretically [1]–[5] and experimentally [6]–[10] as a potential alternative to conventional disk-loaded copper structures. A DLA structure has a simple geometry comprising a dielectric tube surrounded by a conducting cylinder. The simplicity of DLA structures offers great advantages for fabrication of high-frequency (>10 GHz) accelerating structures, as compared with conventional metallic structures which demand extremely tight fabrication tolerances. This is of great importance in the case of linear colliders, where tens of thousands of accelerating structures have to be built. Moreover, the relatively small diameter of DLA structures facilitates the use of quadrupole lenses around the structures. The beam-induced deflection modes [11], [12] for the DLA structures can be effectively damped with a segmented outer conductor wrapped with radio frequency (RF) absorbing material. However, there are still some potential challenges for DLA structures in a high-power RF environment, such as dielectric breakdown [13], thermal heating, and multipactor [14]–[17]. In dielectric breakdown studies, a dielectric surface field breakdown threshold of 13.8 GV/m [18] has been observed at terahertz regime. No breakdown was observed at accelerating gradients of 8 [13], 15 [14], and 18 MV/m [17], respectively, in preceding high-power tests on *X*-band DLA structures. A coating material on the dielectric surface with a high thermal conductivity can effectively transfer heat to the outer copper jacket connected to the cooling system. Surface resonant multipactor has been always observed in experimental studies of the absorption of a large fraction of the incident RF power, which is identified as an issue limiting the gradient in DLA structures. An effective approach that uses an applied axial magnetic field to completely suppress this multipactor in DLA structures has been proposed [15] and demonstrated [16], [17] in high-power experimental studies. The axial magnetic fields may couple the two transverse planes and would hence be unsuitable for many accelerators. The multipactor effect can also be suppressed through the coating of TiN material on the inner surface of the dielectric to reduce the secondary emission coefficient [19].

In addition to these potential challenges, a practical issue to be addressed is the efficient coupling of the RF power into a DLA structure with an outer diameter much smaller than the rectangular waveguide. A scheme [20] using a combination of a side coupling slot and a tapered dielectric layer near the slot was proposed to couple the RF power from a rectangular waveguide into the DLA structure. The tapered dielectric matching section is a part of the DLA structure. It converts TE_{10} mode from a rectangular waveguide to TM_{01} mode in the circular dielectric-loaded waveguide. A power coupling coefficient (it is defined by $\eta = 10^{(S_{21}/10)}$ with S_{21} in decibel and frequently used in the analysis in this article) greater than 95% can be achieved by carefully tuning the coupling slot

Manuscript received February 2, 2022; revised March 8, 2022; accepted March 8, 2022. Date of publication March 11, 2022; date of current version May 18, 2022.

Yelong Wei and Alexej Grudiev are with the RF Group of Accelerator Systems Department, European Organization for Nuclear Research (CERN), 1211 Geneva, Switzerland (e-mail: yelong.wei@cern.ch; alexej.grudiev@cern.ch).

Ben Freemire is with Euclid Techlabs LLC, Bolingbrook, IL 60440 USA (e-mail: b.freemire@euclidtechlabs.com).

Chunguang Jing is with Euclid Techlabs LLC, Bolingbrook, IL 60440 USA, and also with High Energy Physics Division, Argonne National Laboratory, Lemont, IL 60439 USA (e-mail: c.jing@euclidtechlabs.com).

Color versions of one or more figures in this article are available at https://doi.org/10.1109/TNS.2022.3159028.

Digital Object Identifier 10.1109/TNS.2022.3159028

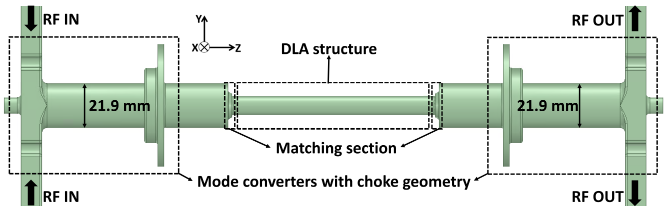

Fig. 1. Conceptual illustration of an externally powered DLA structure, two TE_{10}-TM_{01} mode converters, and two matching sections.

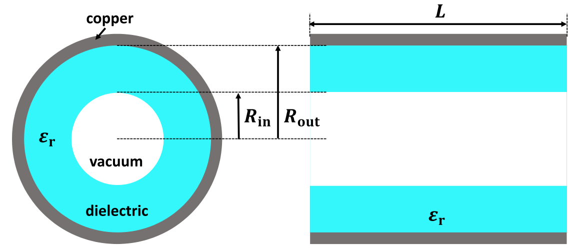

Fig. 2. Front view and longitudinal cross section of a cylindrical DLA structure. ε_r, R_{in}, R_{out}, and L represent the dielectric constant, inner radius, outer radius, and length for the DLA structure, respectively.

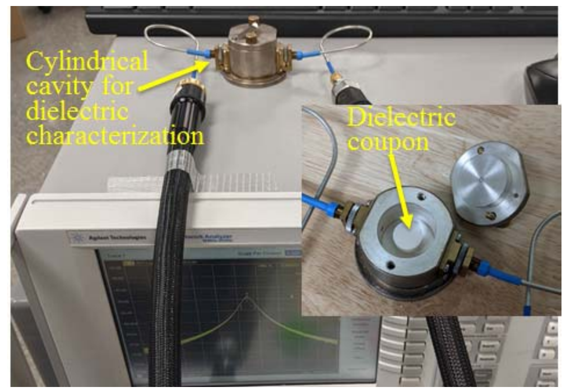

Fig. 3. Setup for measuring the dielectric properties of the material sample.

and tapering the inner radius of the dielectric tube near the coupling slot. However, breakdown was observed for such an RF coupler in the high-power test because of the strong electric field enhancement near the slot [21]. In order to eliminate any field enhancement near the RF coupler due to the presence of dielectrics, another coupling scheme was adopted to separate the RF coupler from the DLA structure [22], [23]. There are two modules in this scheme: an RF coupler section and a tapered dielectric matching section. The RF coupling section is used to convert the TE_{10} mode from a rectangular waveguide to the TM_{01} mode in a circular waveguide. The tapered dielectric section provides a good match for the impedance of the TM_{01} mode between the circular waveguide and the dielectric-loaded waveguide. This scheme separates the dielectric-loaded waveguide from the RF coupler by a tapered matching section and thus makes the RF coupler independent of the dielectric properties. The area of the coupling slot is also much larger, enabling RF fields in the coupling slot much lower than that in the former scheme, under the same input power. Such a tapered dielectric matching section has been used for many high-power experimental studies [8], [13], [14], [16], [17]. In [8] and [16], strong multipactor was observed in a tapered dielectric matching section with a length of >30 mm. At this length, it is a significant challenge to completely suppress multipactor, requiring a large solenoidal magnet capable of producing a uniform axial magnetic field over the whole DLA structure with a tapered dielectric matching section. This length also occupies valuable space, which could be saved for accelerating structures. Thus, a compact matching section with a much shorter length would, if realized, represent an advance for externally powered DLA structures.

Motivated by these points, we present in this article a novel design of matching section to efficiently couple the RF power from a circular waveguide to an X-band DLA structure. There are also two modules in our RF coupling scheme, as shown in Fig. 1. The mode converter has been studied in detail [24], so we concentrate our efforts on the design of the matching section. Section II presents detailed studies for a DLA structure with a dielectric constant $\varepsilon_r = 16.66$ and a loss tangent $\tan\delta = 3.43 \times 10^{-5}$. Section III describes the RF design for a dielectric matching section to achieve the best coupling with the maximum fields located at the DLA structure. Section IV investigates the chamfer of a sharp dielectric corner and a microscale vacuum gap caused by metallic clamping from the point of view of fabrication. Section V shows the tolerance studies for the geometrical parameters of the matching section. Section VI gives the RF performance for the mechanical full-assembly structure, including the DLA structure connected with two matching sections, circular waveguides with choked flanges, and the TE_{10}-TM_{01} mode converters.

II. Design of a DLA Structure

In this section, the RF properties of a DLA structure are studied in detail. A DLA structure comprises a uniform linear dielectric tube surrounded by a copper cylinder, as shown in Fig. 2. Unlike conventional metallic accelerating structures, the uniform DLA structure does not have any geometrical periodicity. By adjusting dielectric constant ε_r, inner radius R_{in}, and outer radius R_{out}, the DLA structure can be operated as a slow wave constant-impedance accelerator. The ceramic materials for dielectric-based accelerating structures have to withstand high-accelerating fields, prevent potential charging by particle beams, have good thermal conductivity, and incur low-power loss. $MgTiO_3$ ceramic, with a dielectric constant $\sim$16 and an ultralow loss tangent $\tan\delta \leq 1.0 \times 10^{-4}$, which has been studied in [25] and [26], is chosen as the dielectric material for such a DLA structure.

An accurate measurement of the dielectric properties has to be performed before using such a material for our RF design. As shown in Fig. 3, a $TE_{01\delta}$ silver-plated resonator [27], [28] with a high quality factor, which is designed for testing ceramics at an X-band frequency, is used to measure the dielectric constant ε_r and loss tangent, $\tan\delta$, of sample coupons. Four dielectric coupons made from the same dielectric rods as for the fabrication of the DLA structure are measured. A dielectric constant $\varepsilon_r = 16.66$ and an ultralow loss tangent $\tan\delta = 3.43 \times 10^{-5}$ (having error bars 0.6% of the nominal value) are

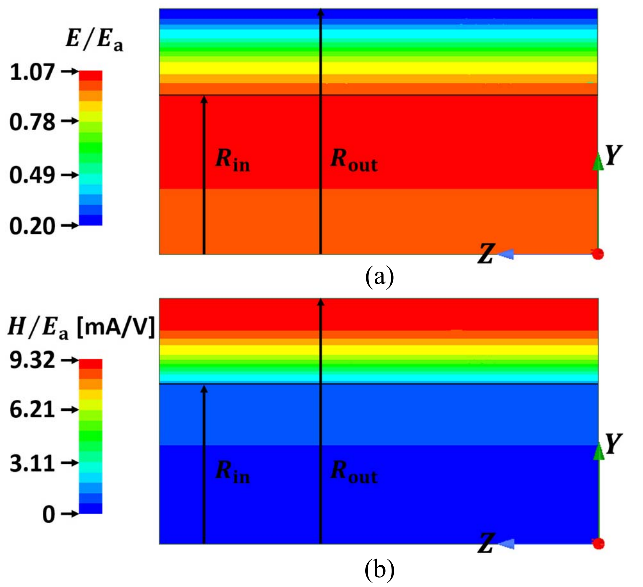

Fig. 4. (a) Electric field distribution E/E_{a} and (b) magnetic field distribution H/E_{a} for the accelerating TM_{01} mode in a DLA structure.

TABLE I
OPTIMUM PARAMETERS FOR A DLA STRUCTURE OPERATING IN TM_{01} MODE

Parameters	A DLA Structure
Dielectric constant ε_r	16.66
Dielectric loss tangent tan δ	3.43×10^{-5}
Inner radius R_{in} [mm]	3.0
Outer radius R_{out} [mm]	4.6388
Length L [mm]	100.0
Acceleration mode	TM_{01}
Frequency f [GHz]	11.994
Unloaded quality factor Q_0	2829
Shunt impedance r'[MΩ/m]	26.5
Group velocity v_g/c	0.066
$E_{\mathrm{s}}/E_{\mathrm{a}}$	1.07
$H_{\mathrm{s}}/E_{\mathrm{a}}$ [mA/V]	9.32
Power required to generate a gradient of 40 MV/m [MW]	45

obtained for the RF design of the DLA structure and matching sections which follows.

HFSS [29] is used to compute the electromagnetic fields for this DLA structure. Peak electric fields and pulsed surface heating [30]–[33] are the two RF constraints to limit the achievable accelerating gradient for the conventional iris-loaded metallic structures. Typically, the ratio of the peak electric field E_{p} to the average accelerating field E_{a} is $E_{\mathrm{p}}/E_{\mathrm{a}} \geq 2$ [34], [35]. Fig. 4 shows the electric field distribution E/E_{a} and magnetic field distribution H/E_{a} of the TM_{01} mode in a DLA structure, where E, E_{a}, and H represent the electric field, the average accelerating field, and the magnetic field, respectively. As shown in Fig. 4(a), the ratio of the peak electric field to the average accelerating field for our DLA structure is calculated to be 1.07. The strongest electric field of $1.07E_{\mathrm{a}}$ is located in the vacuum region next to the dielectric surface while the axial electric field is E_{a}. This slight difference along the y-axis allows the accelerating fields in the vacuum region to be almost identical and uniform. Fig. 4(b) shows that for the same DLA structure, the ratio of the peak magnetic field to the average accelerating field is 9.32 mA/V, which is much larger than that of the existing metallic CLIC-G [36]–[38] structures. It is also found that strong magnetic fields are located on the metallic surface, resulting in large surface currents and hence high-power loss and high-pulsed surface heating temperature rise [30]–[33]. For the similar pulsed temperature rise of <56 K as that of CLIC-G structures, the maximum achievable gradient is calculated to be 62 MV/m for this DLA structure. However, no dielectric breakdown caused by RF pulsed heating was observed in preceding high-power tests. This is probably because the gradients for DLA structures are usually limited to 10–20 MV/m [13], [14], [16], [17] due to surface multipactor. Therefore, the following studies focus on the analysis of electric fields only for the design of a dielectric matching section.

Table I shows all the geometrical and RF parameters for our DLA structure operating in TM_{01} mode. The inner radius is chosen to be 3.0 mm from consideration of the beam dynamics requirement of CLIC designs [36]–[38]. The outer radius is then calculated to be 4.6388 mm for an operating frequency of $f_0 = 11.994$ GHz. The group velocity obtained is $v_g = 0.066c$, where c is the speed of light. An unloaded quality factor of $Q_0 = 2829$ and a shunt impedance of $R_{\mathrm{shunt}} = 26.5$ MΩ/m are also derived for such a DLA structure. Both RF parameters are much less advantageous when compared to the existing metallic CLIC [36]–[38] structures, agreeing with the prediction of a large $H_{\mathrm{p}}/E_{\mathrm{a}} = 9.32$ mA/V. It is expected that a gradient of 40 MV/m can be generated for this DLA structure at an input power of 45 MW from XBOX facility [39], [40]. Due to the compromise between cost and fabrication difficulty, the length of the DLA structure is chosen as 100 mm for the following simulations and mechanical assembly.

III. DESIGN OF A COMPACT DIELECTRIC MATCHING SECTION

Simulation studies [41] have shown that a good match can be achieved for the impedance of the TM_{01} mode between the circular waveguide and the dielectric-loaded waveguide by using a vacuum-waveguide quarter-wavelength matching section. However, there is an issue with very high electromagnetic fields located in the vacuum-waveguide matching section due to the strong resonance within it. In addition, it has a very narrow bandwidth. As a solution, a compact dielectric disk is therefore added into the vacuum matching section. In this section, a dielectric-based quarter-wavelength matching section to efficiently couple RF power from a circular waveguide into the DLA structure will be proposed and studied in detail.

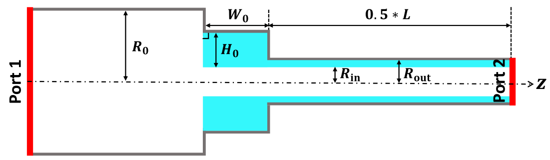

Fig. 5. Longitudinal cross section of a circular waveguide, a cylindrical matching section, and a DLA structure.

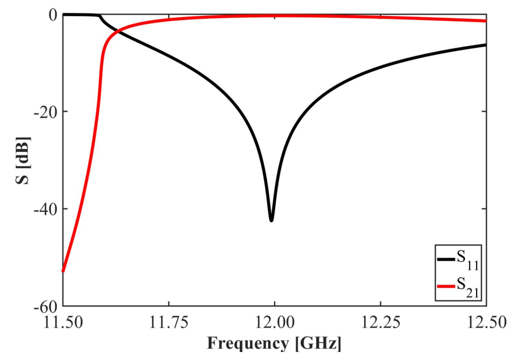

Fig. 6. Simulated S_{11} and S_{21} as a function of frequency for the geometry shown in Fig. 5.

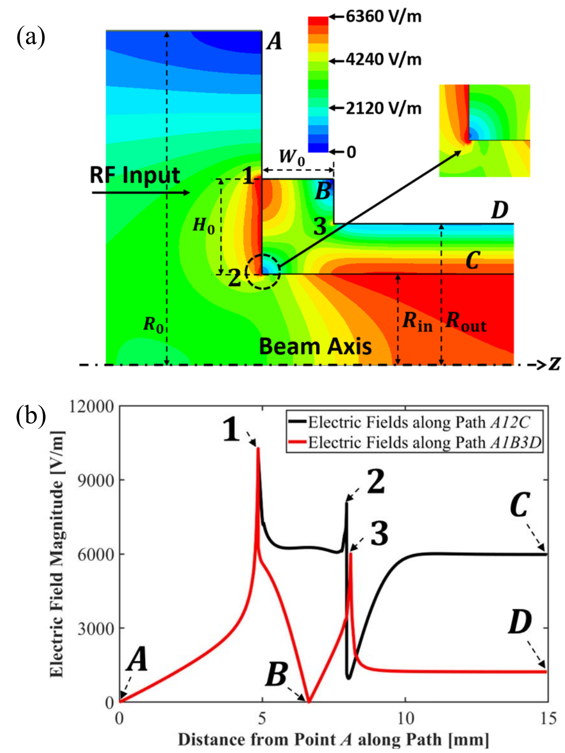

Fig. 7. (a) Electric field distribution for the geometry shown in Fig. 5. (b) Electric field magnitude along Paths *A12C* and *A1B3D*. Paths *A12C* and *A1B3D* denoted directed paths starting at point *A* and defined by the straight line segments between points *A*, 1, 2, and *C* and points *A*, 1, *B*, 3, and *D*, respectively.

A. Cylindrical Matching Section

The DLA structure has the geometry listed in Table I. Fig. 5 shows the dielectric matching section, which consists of a dielectric cylindrical tube with right-angle profile corners. The dielectric material is exactly the same as for the DLA structure. This matching section has a width W_0 and a height H_0 for a fixed $R_{\text{in}} = 3.0$ mm. There are two waveguide ports (Ports 1 and 2, see Fig. 5) defined for the calculation of *S*-parameters in HFSS simulations. The desired reflection coefficient S_{11} and transmission coefficient S_{21} can be realized by tuning the values of W_0 and H_0. The goal of the optimization is to achieve $S_{11} \leq -20$ dB and $S_{21} \geq -1$ dB at the operating frequency of 11.994 GHz for the following studies. Such an $S_{21} \geq -1$ dB corresponds to a coupling coefficient of $\eta \geq 80\%$.

After optimization, the values of $S_{11} = -42$ dB and $S_{21} = -0.33$ dB are achieved at the operating frequency of 11.994 GHz for a dielectric matching section with $W_0 = 1.777$ mm and $H_0 = 3.1$ mm, as shown in Fig. 6. This dielectric matching section has a width much smaller than that of previously reported tapered matching sections [22], [23], since it is based on different matching mechanism: a quarter-wavelength transformer. The $S_{11} = -42$ dB indicates that the reflected RF power is negligibly small. Using $S_{21} = -0.33$ dB, the coupling coefficient is calculated to be 93%. S_{21} also has a broad 3-dB bandwidth of more than 1.0 GHz, which allows greater tolerance to potential fabrication errors. It should be noted here that this 3-dB bandwidth is not centered at the operating frequency due to the proximity of the cutoff to the left in Fig. 6. This compact cylindrical matching section is expected to be efficient.

After simulating *S*-parameters, we investigated the RF field distribution for this cylindrical dielectric matching section. Only electric fields are analyzed here because it is they which limit the achievable accelerating gradient for the DLA structures. Fig. 7(a) shows the electric field distribution for the dielectric matching section connected to a circular waveguide and a DLA structure, at an input power of 1.0 W. It is found that very strong fields are located at three corners denoted by the numbers 1–3, as shown in Fig. 7(a). Fig. 7(b) shows the electric field magnitude along Paths *A12C* and *A1B3D* [see Fig. 7(a)]. A total of three peaks are observed in these black and red curves, corresponding to the strong fields at Corners 1–3. The strong fields at these three corners will result in dielectric breakdown in the high-power tests. Solutions are required to reduce these strong fields below those of the DLA structure, which is the goal of the optimization in terms of fields.

B. Truncated Conical Matching Section

In order to reduce the peak fields at Corner 1, the dielectric matching section with right-angle profile corners can be changed to a truncated conical dielectric matching section, as shown in Fig. 8. It has four geometrical parameters: a width $W_1 = W_0$, an upper height H_1, a lower height H_2, $H_0 = H_1 + H_2$, and a base angle θ. Based on $\tan\theta = (W_1/H_1)$, when two arbitrary variables are selected from W_1, H_1, and θ, the remaining one is fixed. The desired *S*-parameters (S_{11} and S_{21}) can be obtained by tuning a combination of H_2 and two of W_1, H_1, and θ.

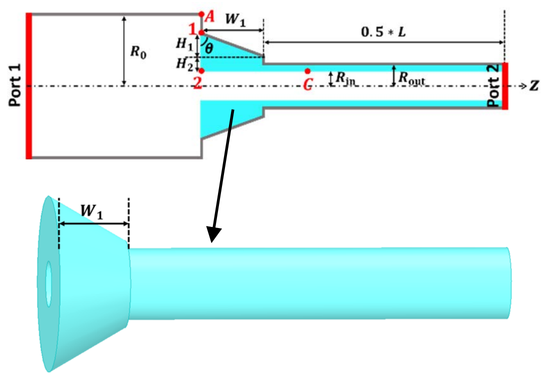

Fig. 8. Longitudinal cross section of a circular waveguide, a dielectric matching section in the shape of a truncated cone, and a DLA structure. Here, Path *A12C* has the same definition, as shown in Fig. 7(a).

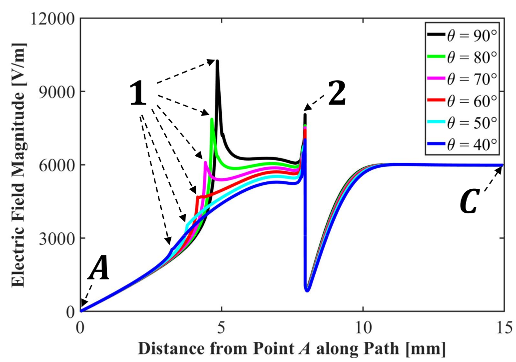

Fig. 9. Electric field magnitude along Path *A12C* (see Fig. 8) for the dielectric matching section, for different base angles.

Fig. 9 shows the calculated electric field magnitude along Path *A12C* (see Fig. 8) for the dielectric matching section for different base angles θ, at an input power of 1.0 W. When $\theta = 90°$, this is the cylindrical case, which has been described in Section III-A. There are two obvious peaks in each simulation. The left peak indicates the strong fields at Corner 1, while the right peak represents the strong fields at Corner 2. As expected for this kind of triple point, it can be clearly seen that the left peak gradually drops with a smaller base angle, while the right peak still exists. For $\theta < 70°$, the peak fields at Corner 1 are reduced below those of the DLA structure, which meets the goal of optimization. A smaller base angle θ also results in a narrower width W_1. A base angle $\theta = 60^{\text{o}}$ is therefore chosen for our dielectric matching section due to a tradeoff between the reduced fields and reasonable width for fabrication.

C. Corner Rounding

As seen in Fig. 9, the peak corresponding to the strong fields located at Corner 2 still exists for a truncated conical dielectric matching section. In order to reduce the peak fields at Corner 2, we round this corner with a filet radius R_{f}. Fig. 10 shows the influence of different filet radii on the electric field magnitude at Corner 2, at an input power of 1.0 W. The peak fields at Corner 2 gradually become weaker with a larger filet radius. A larger filet radius of $R_{\text{f}} \geq 2.5$ mm results in a thinner

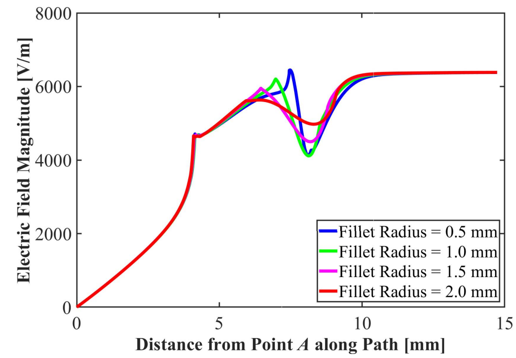

Fig. 10. Electric field magnitude along Path *A1C* [see Fig. 11(a)] for different filet radii at Corner 2.

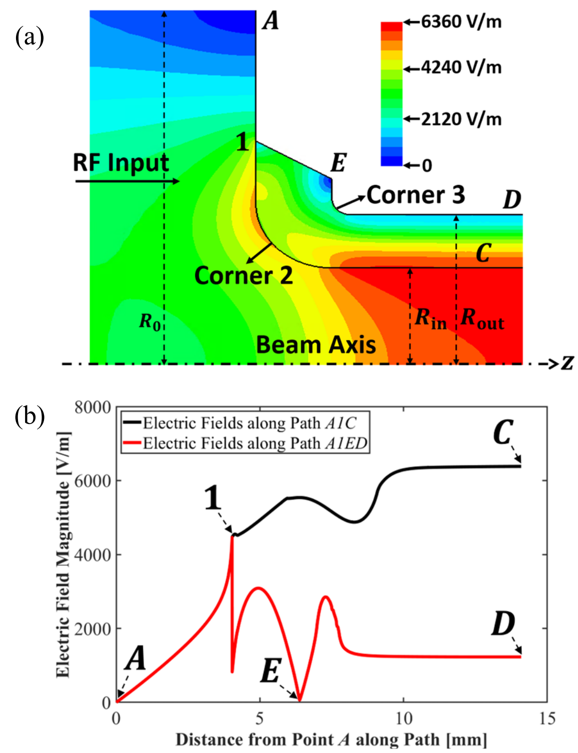

Fig. 11. (a) Electric field distribution for a truncated conical dielectric matching section. (b) Electric field magnitude along Paths *A1C* and *A1ED*. Paths *A1C* and *A1ED* denoted directed paths starting at point *A* and defined by the straight line and curved segments between points *A*, 1, and *C* and points *A*, 1, *E*, and *D*, respectively.

matching section, which may bring difficulty for fabrication. For a filet radius of $R_{\text{f}} \geq 1.5$ mm, the electric fields at both Corners 1 and 2 are reduced lower than those of the DLA structure. Therefore, a filet radius of $R_{\text{f}} = 2.0$ mm is chosen due to a tradeoff between the reduced fields and reasonable thickness for fabrication.

A similar rounding method is also applied for Corner 3 with a filet radius of $R_{\text{m}} = 0.5$ mm. After such a rounding, we find the electric field distribution shown in Fig. 11(a) in the matching section at an input power of 1.0 W. The electric fields at Corner 3 are much weaker than those of the DLA structure, as shown in red curve of Fig. 11(b). In this case, such

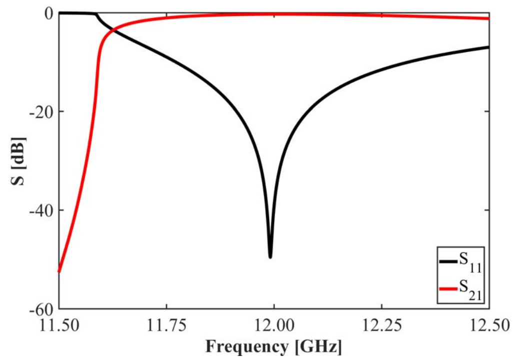

Fig. 12. Simulated S_{11} and S_{21} as a function of frequency for an optimum dielectric matching section.

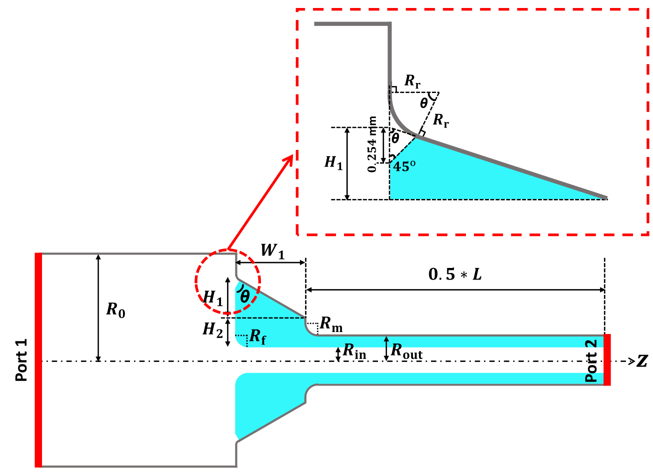

Fig. 13. Longitudinal cross section of a circular waveguide, a dielectric matching section with a chamfered corner, and a DLA structure.

a dielectric matching section has the potential to survive in a high gradient of 15 [14] and 18 MV/m [17], as the maximum electric fields are located in the DLA structure, and does not limit the high gradient performance of the DLA structure itself.

For a dielectric matching section with a base angle of $\theta = 60^{\text{o}}$, and rounded Corners 2 and 3 with filet radii of $R_{\text{f}} = 2.0$ mm and $R_{\text{m}} = 0.5$ mm, respectively, an optimum geometry can be found by sweeping different widths W_1 and lower heights H_2 together, to provide a good matching between the circular waveguide and the DLA structure. Fig. 12 shows the calculated $S_{11} = -48$ dB and $S_{21} = -0.31$ dB for an optimum dielectric matching section with a width of $W_1 = 2.031$ mm and a lower height of $H_2 = 2.743$ mm, at the operating frequency of 11.994 GHz. Both S_{11} and S_{21} are almost exactly the same as for the matching section with right-angle profile corners. It has a coupling coefficient of 93% and S_{21} also has a broad 3-dB bandwidth of more than 1.0 GHz.

IV. Considerations for Fabrication Studies

In this section, we take fabrication requirements into account for our design. These fabrication requirements, including chamfers on sharp dielectric corners and the existence of microscale vacuum gaps caused by metallic clamping, are studied in simulations.

A. Chamfered Corner

In the fabrication of the dielectric matching section, a sharp corner easily breaks. In order to prevent such a break, a 45° chamfer with a length of 0.254 mm is added for the sharp dielectric corner, as shown in Fig. 13. The shape of the outer metal is also changed by rounding with a filet radius of $R_{\text{r}} = 0.322$ mm, in order to prevent field enhancement near that area. The width W_1, the upper height H_1, and the lower height H_2 of the dielectric matching section are thereby adjusted for the best matching performance and RF field distribution.

After chamfering the sharp dielectric corner, a dielectric matching section is therefore obtained as follows: $W_1 = 2.035$ mm, $H_2 = 2.74$ mm, $\theta = 60°$, $R_{\text{f}} = 2.0$ mm, and $R_{\text{m}} = 0.5$ mm. Fig. 14(a) shows the calculated electric field distribution for a dielectric matching section with a chamfered corner at an input power of 1.0 W. Fig. 14(b) indicates that

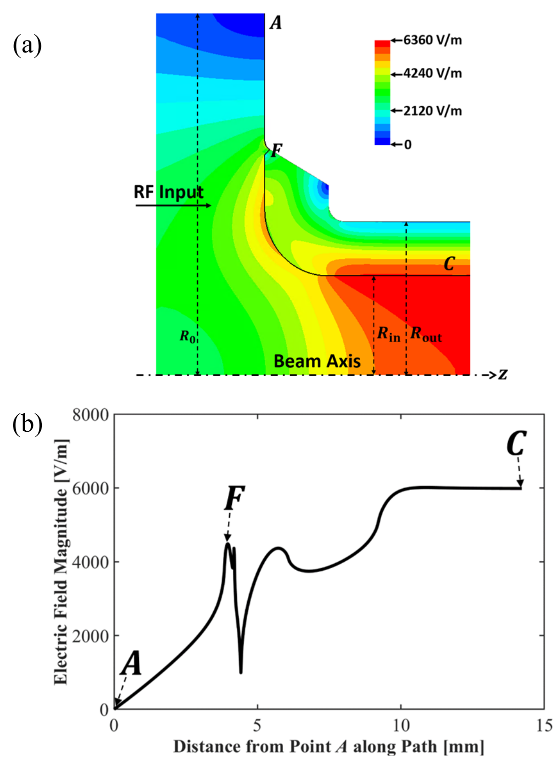

Fig. 14. (a) Electric field distribution for the matching section with a chamfered corner. (b) Electric field magnitude along Path AFC, which denoted directed paths starting at point A and defined by the straight line and curved segments between points A, F, and C.

the electric fields located in such a matching section are significantly lower than those of the DLA structure. This is the ideal case for future high-power tests on our DLA structure.

Fig. 15 shows the simulated $S_{11} = -48$ dB and $S_{21} = -0.31$ dB for the matching section with a chamfered corner at the operating frequency of 11.994 GHz. Both S_{11} and S_{21} are exactly the same as those of the optimum matching section. S_{21} also has a broad 3-dB bandwidth of more than 1.0 GHz, which allows greater tolerance to potential fabrication errors.

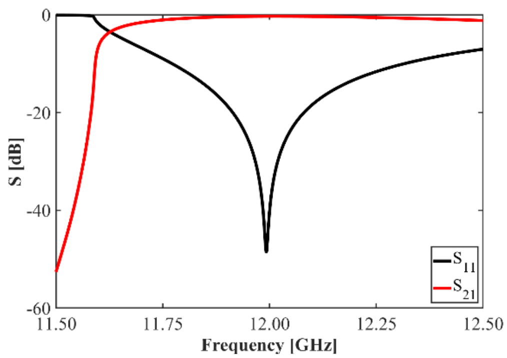

Fig. 15. Simulated S_{11} and S_{21} as a function of frequency for the matching section with a chamfered corner.

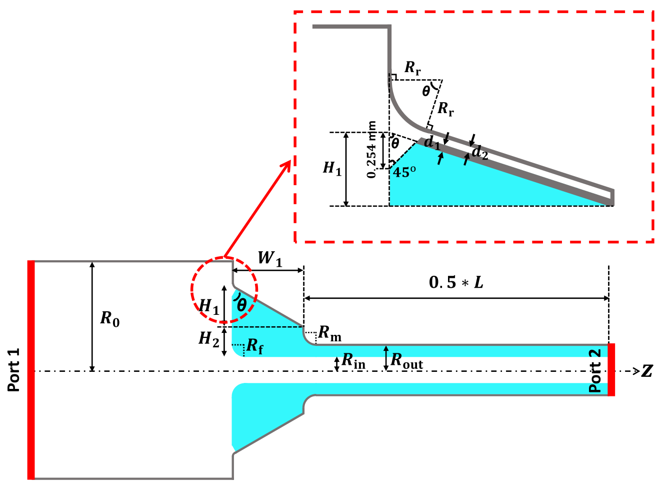

Fig. 16. Longitudinal cross section of a circular waveguide, a dielectric matching section with a vacuum microgap, and a DLA structure.

B. Vacuum Microgap

It was found [13] that any microgap caused by a dielectric joint resulted in RF breakdown, due to strong field enhancement. In our fabrication, the entire dielectric tube, including the matching section and the DLA structure, is machined as a single piece. A thin metallic layer of 0.0508 mm is first coated onto the surface of the whole dielectric tube through physical vapor deposition in order to keep in close touch with the outer copper jacket. The coated dielectric tube is then inserted into the outer copper jacket. However, there is still a microscale vacuum gap caused by metallic clamping between the thin metallic coating and the outer thick copper jacket, as shown in Fig. 16. It is therefore of particular importance to study the dependence of the S-parameters and electric fields on this microgap d_2.

Fig. 17 shows how the vacuum microgap d_2 influences S_{11} and S_{21}. With a larger design gap, S_{11} increases while S_{21} remains almost unchanged, resulting in worse matching. For a vacuum microgap of $d_2 = 0.2$ mm, $S_{11} = -31.5$ dB and $S_{21} = -0.31$ dB are obtained. S_{11} is increased to -28 dB and S_{21} stays almost constant, when the vacuum microgap becomes 0.3 mm.

Fig. 18(a) shows the calculated electric field distribution for the matching section with a vacuum microgap, at an input power of 1.0 W. Fig. 18(b) gives the calculated electric field magnitude along Path AGC for different vacuum microgaps.

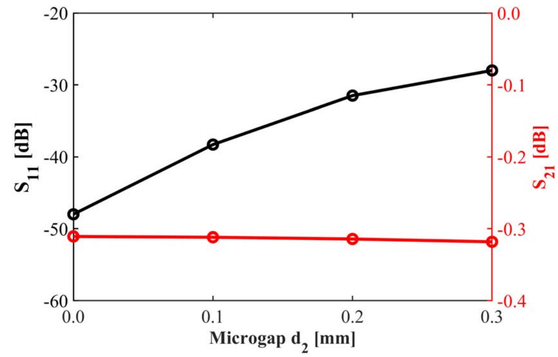

Fig. 17. Simulated S_{11} and S_{21} as a function of vacuum microgap d_2.

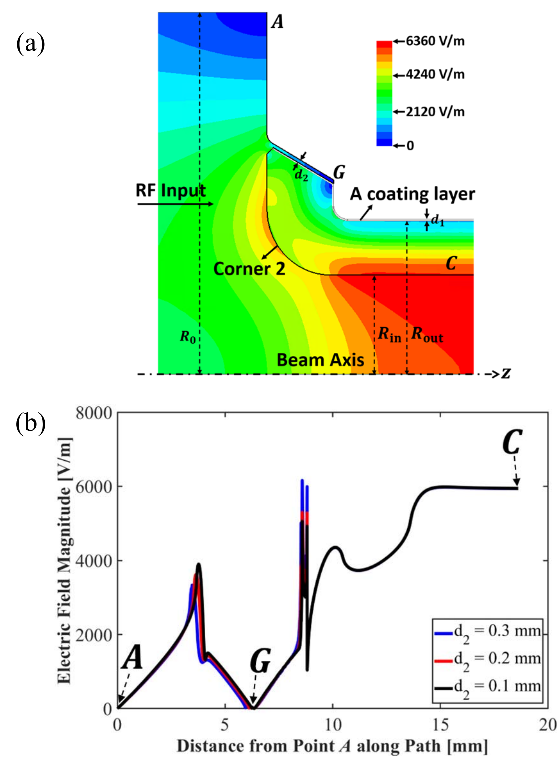

Fig. 18. (a) Electric field distribution for a dielectric matching section with a vacuum microgap d_2, where a thin metallic coating layer is denoted by the white lines. (b) Electric field magnitude along Path AGC for different vacuum microgaps d_2. Path AGC denoted directed paths starting at point A and defined by the straight line and curved segments between points A, G, and C.

There are two peaks in each curve, indicating the relatively strong fields near the chamfered corner and rounding Corner 2, respectively. For a vacuum microgap of 0.3 mm, the peak fields are higher than those of the DLA structure, which may cause arcing in a high-power test. The dielectric matching section is therefore allowed to have a maximum microgap of 0.2 mm, in which RF fields are still lower than those of the DLA structure. This value is used to guide the fabrication tolerances of the copper jacket and the metallic coating of the dielectric tube.

V. Tolerance Studies

Assuming microgap $d_2 = 0$ mm, geometrical parameters for the dielectric matching section and the DLA structure

TABLE II
TOLERANCES OF GEOMETRICAL PARAMETERS FOR THE DLA STRUCTURE WITH A DIELECTRIC MATCHING SECTION

$f_0 = 11.994$ GHz	$S_{11} \le -20$ dB
$\varepsilon_r = 16.66$	[-0.24, +0.27]
$W_1 = 2.035$ [mm]	[-0.022, +0.022]
$H_2 = 2.74$ [mm]	[-0.051, +0.054]
$\theta = 60^o$	[-7.3º, +7.0º]
$R_f = 2.0$ [mm]	[-0.140, +0.120]
$R_m = 0.5$ [mm]	[-0.245, +0.151]
$R_{out} = 4.6388$ [mm]	[-0.020, +0.025]
$R_{in} = 3.0$ [mm]	[-0.024, +0.020]
$d_2 = 0$ [mm]	[0, +0.2]

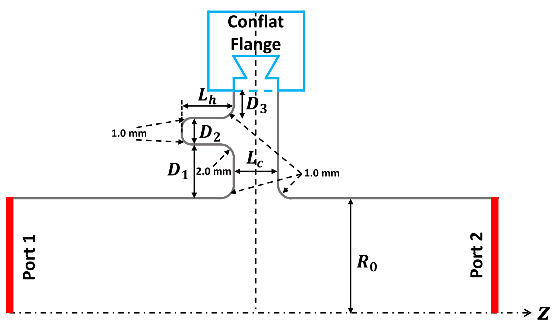

Fig. 19. Longitudinal cross section of a circular waveguide with a choke geometry.

(see Fig. 13) are obtained as follows: $\varepsilon_r = 16.66$, $W_1 = 2.035$ mm, $H_2 = 2.74$ mm, $\theta = 60°$, $R_f = 2.0$ mm, $R_m = 0.5$ mm, $R_{out} = 4.6388$ mm, $R_{in} = 3.0$ mm, and $L = 100$ mm. Using these geometrical parameters, $S_{11} = -48$ dB and $S_{21} = -0.31$ dB are achieved at the operating frequency of 11.994 GHz.

As shown in Fig. 15, S_{21} for the matching section has a large 3-dB bandwidth of over 1 GHz, so it is not sensitive to changes in the geometrical parameters. The tolerances are studied by calculating the dependence of S_{11} on the geometrical parameters. By adjusting each geometrical parameter in turn from x to $x \pm dx$ until S_{11} rises above -20 dB, the permissible variation of the parameter is determined. The length of the DLA structure affects S_{21} due to RF power loss in the dielectrics and metallic surface, but it does not have any effect on the S_{11} and RF-field performance, so it is ruled out for tolerance studies in this section. The tolerances of key geometrical parameters (see Table II) are discussed in detail. It should be noted here that values in bracket (see Table II) represent absolute deviations.

Using the data in Table II, it is seen that the strictest constraints are on W_1, R_{out}, and R_{in}, while H_2, θ, R_f, R_m, and d_2 have wider tolerances. The dielectric fabrication accuracy should be better than ± 0.02 mm in order to realize an $S_{11} \le -20$ dB. It should be noted here that these tolerances are effects of individual geometrical parameters. When multiple parameters are varied simultaneously including a vacuum gap of $d_2 = 0.2$ mm, it may result in worse S_{11} and S_{21}. The acceptance criteria for coupling coefficient are assumed to be $\eta \ge 80\%$ in this article. In the worst case, S_{21} is found to be $S_{21} \ge -0.45$ dB, enabling the coupling coefficient of 90%. This is acceptable for efficient coupling for high-power experiments on DLA structures.

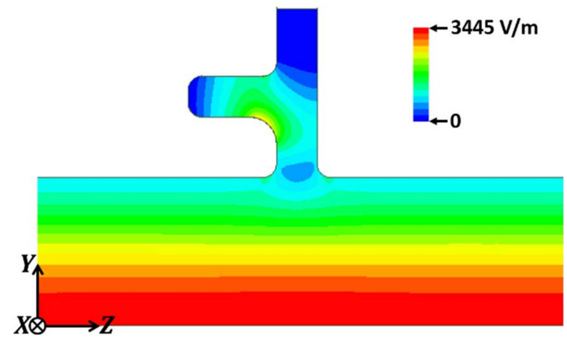

Fig. 20. Electric field distribution for the accelerating mode TM_{01} in a circular waveguide with a choke geometry.

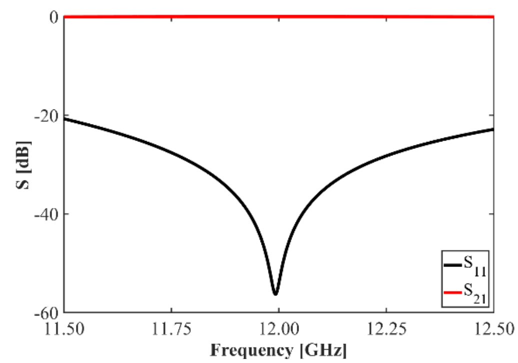

Fig. 21. Simulated S_{11} and S_{21} as a function of frequency for a choke geometry connected to a circular waveguide, as shown in Fig. 19.

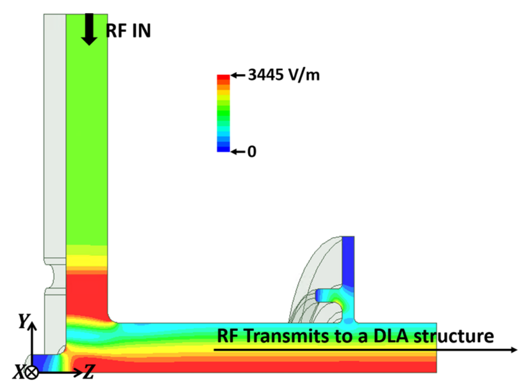

Fig. 22. Electric field distribution for the TE_{10}-TM_{01} mode converter with a choke geometry.

VI. FULL-ASSEMBLY STRUCTURE

In this section, a full-assembly structure is obtained by adding the DLA structure connected together with two matching sections, circular waveguides with choked flanges, and the

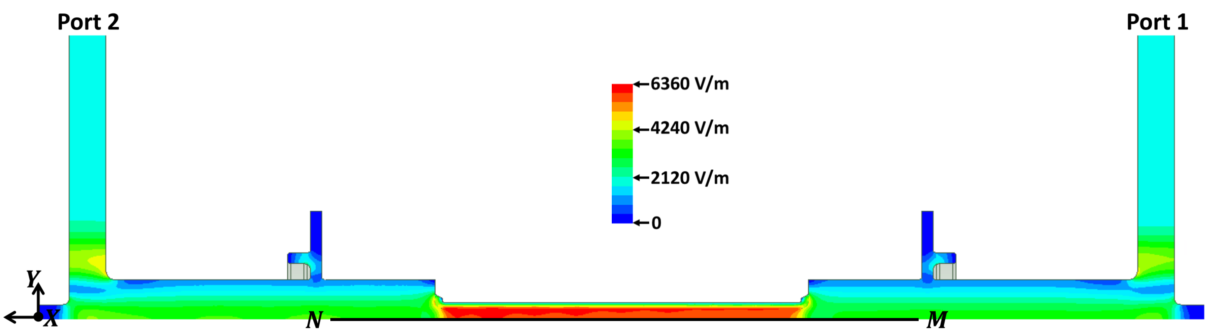

Fig. 23. Electric field distribution for the full-assembly structure, where line *MN* is located on the center along the z-axis.

TE_{10}-TM_{01} mode converters. The RF performance of such a full-assembly structure is described in detail.

A. Choke Geometry

In order to remove the contact issue for assembling two parts together, a choke geometry is added, as shown in Fig. 19. In this case, the disks have no bonding joints in high RF fields. There are five geometrical parameters (D_1, D_2, D_3, L_c, and L_h) for a choke geometry. Through proper design, this choke can be used to reflect the fundamental TM_{01} mode back to the circular waveguide, so that it will not affect the RF fields traveling in the circular waveguide. A conflat flange, located outside, is used to assemble both of the circular vacuum waveguides tightly together.

Based on simulations [42], a choke with geometrical dimensions is obtained: $D_1 = 4.5$ mm, $D_2 = 3.0$ mm, $D_2 \geq 5.0$ mm, $L_c = 3.0$ mm, and $L_h = 6.535$ mm. Filet radii are also added to round all of the corners, as shown in Fig. 20. Fig. 20 shows the electric field distribution for the fundamental TM_{01} mode in a circular waveguide with this optimum choke, at an input power of 1.0 W. It can be clearly seen that the electric fields in such an optimum choke are much weaker than those in the circular waveguide. This indicates that the choke should not affect the high-power performance of the circular waveguide for operation in TM_{01} mode.

Fig. 21 gives the calculated values of $S_{11} = -56$ dB and $S_{21} = -0.01$ dB for a circular waveguide with a choke geometry, at an operating frequency of 11.994 GHz. This means that 99.8% of RF power is transmitted from Port 1 to Port 2 (see Fig. 19) and 0.2% of RF power is dissipated on the metallic surface and choke structure. The choke has a negligible effect on the RF power transmitted in the circular waveguide. In addition, the transmission coefficient S_{21} for this choke has a very broad 3-dB bandwidth of more than 3 GHz. This allows flexibility in the fabrication and mechanical assembly requirements for a choke geometry.

B. TE_{10}-TM_{01} Mode Converter

A TE_{10}-TM_{01} mode converter at a frequency of 11.994 GHz has been studied at CERN [24]. It is used to efficiently convert the TE_{10} mode from a rectangular waveguide to the TM_{01} mode in a circular waveguide. Fig. 22 shows the calculated

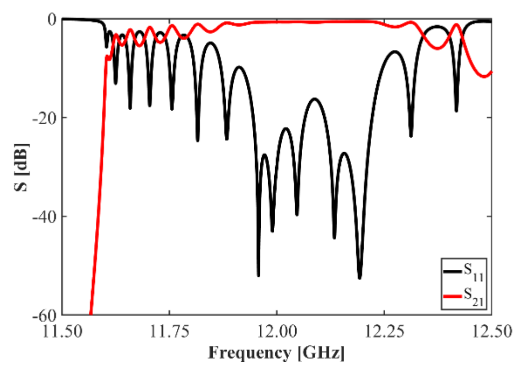

Fig. 24. Simulated S_{11} and S_{21} as a function of frequency for the full-assembly structure shown in Fig. 23.

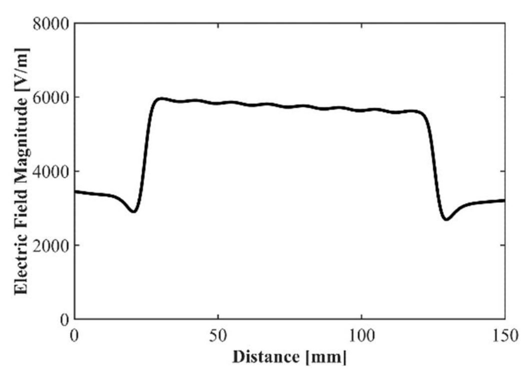

Fig. 25. Electric field magnitude along the line *MN* shown in Fig. 23. The distance of point *M* is taken as 0 mm.

electric field distribution for the mode converter connected with a choke geometry at an input power of 1.0 W.

C. Full-Assembly Structure

By using the mode converters, together with a choke geometry, the dielectric matching section, and the DLA structure, a full-assembly structure, as shown in Fig. 23, is obtained. We simulate the whole structure by analyzing the electric field distribution and S-parameters from Port 1 to Port 2. RF power loss, on both the metallic surface and in dielectrics and accelerating fields in the vacuum channel, is also studied in detail.

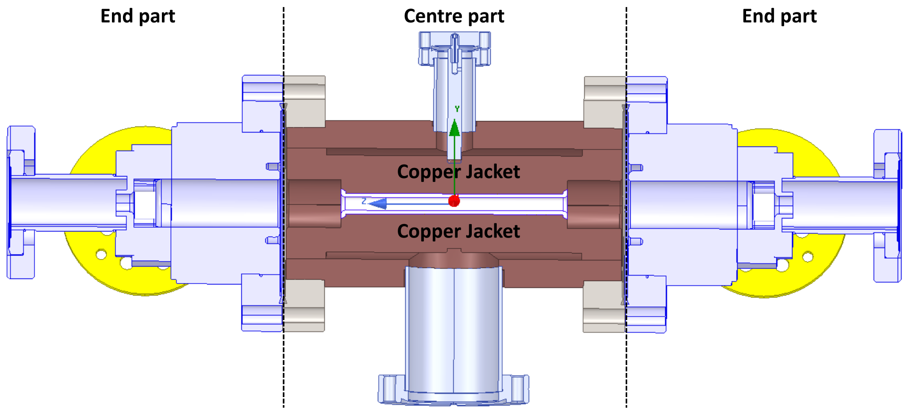

Fig. 26. Full-assembly mechanical design for the whole structure, including a center part and two end parts.

Fig. 24 gives the calculated values of $S_{11} = -40$ dB and $S_{21} = -0.67$ dB for the full-assembly structure at the operating frequency of 11.994 GHz. When the dielectric matching section has geometrical errors as listed in Table II, $S_{11} \leq -20$ dB and $S_{21} \geq -1$ dB can still be achieved for such a full-assembly structure. Using the power density on the metallic surface and in the dielectric area for an input power of 1.0 W, the calculated RF power loss on the metallic surface is $P_{\text{loss\_surface}} = 0.130$ W and the RF power loss obtained in dielectrics is $P_{\text{loss\_dielectric}} = 0.012$ W. So, the total RF power loss is $P_{\text{total\_loss}} = 0.142$ W. The output RF power at Port 2 is $P_{\text{out}} = 0.858$ W. We thus achieve a transmission coefficient $S_{21} = 10 \log (P_{\text{out}}/P_{\text{in}}) = -0.67$ dB, which agrees well with the simulated S_{21} shown in Fig. 24. At the maximum peak power of 45 MW from XBOX facility [39], [40] with a pulsewidth of 1.2 μs and a repetition rate of 50 Hz, it corresponds to an average input power of 2.7 kW. The power loss on the metallic surface is then 351 W and the power loss in dielectrics is 32.4 W. A water cooling system is thus required for the high-power test on the full-assembly structure.

Fig. 25 shows the electric field magnitude along a line *MN* (see Fig. 23). The electric fields are gradually becoming weaker, due to RF power loss in the dielectric and on metallic surfaces, as the RF fields propagate from point *M* to point *N*. The average accelerating gradient is calculated to be 5773 V/m at an input power of 1.0 W. For a power of 45 MW from XBOX facility [39], [40], an average accelerating gradient of 40 MV/m can be achieved for our DLA structure.

Fig. 26 presents the full-assembly mechanical design for the whole structure. The gray area denotes the outer copper jacket, connected with openings to avoid air trapping when pumping. Two conflat flanges are used to connect the center part with the end parts, which are TE_{10}-TM_{01} mode converters.

VII. Conclusion

In this article, a compact, low-field, broadband dielectric matching section has been proposed and studied to efficiently couple the RF power from a circular waveguide to an *X*-band DLA structure. Through simulation studies, an optimum dielectric matching section with a chamfered corner is obtained: $\theta = 60^\circ$, $W_1 = 2.035$ mm, and $H_2 = 2.74$ mm, achieving a reflection coefficient of $S_{11} = -48$ dB and a transmission coefficient of $S_{21} = -0.31$ dB with a very broad 3 dB width of more than 1 GHz. This dielectric matching section is much more compact than the previous ones with a length of >30 mm [8], [16] for DLA structures. Therefore, this dielectric matching section would be very advantageous, given that it saves the valuable space for the DLA structures.

It is also found that the maximum allowable size for any microscale vacuum gap caused by metallic clamping between a thin metallic coating and the outer thick copper jacket is 0.2 mm. Tolerance studies show that the dielectric fabrication accuracy should be better than ± 0.02 mm in order to realize a $S_{11} \leq -20$ dB. Finally, a full-assembly structure, including the DLA structure connected with two matching sections, circular waveguides with choked flanges, and the TE_{10}-TM_{01} mode converters, is analyzed in detail. $S_{11} = -40$ dB and $S_{21} = -0.67$ dB are obtained in simulation for this full-assembly structure. For a power of 45 MW from XBOX facility [39], [40], an average accelerating gradient of 40 MV/m can be expected for our DLA structure.

There are still some potential issues for fabrication processing and high-power tests on the DLA structures with a compact matching section. It is very challenging to achieve a fabrication accuracy of ± 0.02 mm as compared to *X*-band copper structures. Measurement techniques need to be introduced during the fabrication processing on the whole dielectric tube. Particular attention should be paid to the physical vapor deposition for achieving a good quality of coating with an even thickness on the outer surface of dielectric tube. The heating of ceramics may affect the RF properties of DLA structures, which is waiting for further experimental studies. It is also foreseen that dielectric RF breakdown [13] and surface resonant multipactor [14]–[17] would be the primary issues to limit the achievable gradient for DLA structures. For our 100-mm DLA structure with two dielectric matching sections, the same solenoid as [16] consisting of a 10.3-cm-long, 168-turn coils with 2.5-cm-thick iron guard at both ends is good enough to fully suppress the surface multipactor. This applied axis magnetic field may couple the two transverse planes for the electron beam. Thus, further studies are required to solve these issues.

Despite these challenging issues, the DLA structures with such a compact matching section have potential real-life applications. For example, for a 100-mm DLA structure with a gradient of 10 MV/m, it may become possible to build a portable lightweight and cost-effective accelerator to deliver ~1-MeV beam dose for therapy [43].

ACKNOWLEDGMENT

The authors would like to thank Dr. Walter Wuensch for the useful comments, the team of Argonne Wakefield Accelerator facility (Dr. Manoel Conde, Dr. John Power, and Dr. Jiahang Shao, etc.) for the fruitful discussions, Dr. Joel Sauza Bedolla for the mechanical design of the mode converters, and Dr. Mark Ibison for his careful reading of the manuscript.

REFERENCES

[1] R. B. R. S. Harvie, "A proposed new form of dielectric-loaded waveguide for linear electron accelerators," *Nature*, vol. 162, no. 4127, p. 890, Dec. 1948.

[2] G. T. Flesher and G. I. Cohn, "Dielectric loading for waveguide linear accelerators," *Trans. Amer. Inst. Electr. Eng.*, vol. 70, no. 1, pp. 887–893, Jul. 1951.

[3] R. B. R.-Shersby-Harvie, L. B. Mullett, W. Walkinshaw, J. S. Bell, and B. G. Loach, "A theoretical and experimental investigation of anisotropic-dielectric-loaded linear electron accelerators," *Proc. IEE B, Radio Electron. Eng.*, vol. 104, no. 15, pp. 273–290, May 1957.

[4] L. Xiao, W. Gai, and X. Sun, "Field analysis of a dielectric-loaded rectangular waveguide accelerating structure," in *Proc. Part. Accel. Conf. (PACS)*, Chicago, IL, USA, 2001, pp. 3963–3965.

[5] C. Jing, W. M. Liu, W. Gai, J. G. Power, and T. Wong, "Mode analysis of a multilayered dielectric-loaded accelerating structure," *Nucl. Instrum. Methods Phys. Res. A, Accel. Spectrom. Detect. Assoc. Equip.*, vol. 539, no. 3, pp. 445–454, Mar. 2005.

[6] G. B. Walker and E. L. Lewis, "Vacuum breakdown in dielectric-loaded wave-guides," *Nature*, vol. 181, no. 4601, pp. 38–39, Jan. 1958.

[7] W. Gai *et al.*, "Experimental demonstration of wake-field effects in dielectric structures," *Phys. Rev. Lett.*, vol. 61, no. 24, pp. 2756–2758, Dec. 1988.

[8] J. G. Power *et al.*, "Observation of multipactor in an alumina-based dielectric-loaded accelerating structure," *Phys. Rev. Lett.*, vol. 92, no. 16, Apr. 2004, Art. no. 164801.

[9] O. Sinitsyn, G. Nusinovich, T. Antonsen, S. H. Gold, and G. S. Nusinovich, "Studies of multipactor in dielectric-loaded accelerator structures: Comparison of simulation results with experimental data," in *Proc. AIP Conf.*, 2010, pp. 302–306.

[10] D. Satoh, M. Yoshida, and N. Hayashizaki, "Fabrication and cold test of dielectric assist accelerating structure," *Phys. Rev. A, Gen. Phys. Beams*, vol. 20, no. 9, Sep. 2017, Art. no. 091302.

[11] W. Gai and C. Ho, "Modeling of the transverse mode suppressor for dielectric wake-field accelerator," *J. Appl. Phys.*, vol. 70, pp. 3955–3957, Oct. 1991.

[12] E. Chojnacki *et al.*, "Measurement of deflection-mode damping in an accelerating structure," *J. Appl. Phys.*, vol. 69, no. 9, pp. 6257–6260, May 1991.

[13] C. Jing *et al.*, "High-power RF tests on X-band external powered dielectric-loaded accelerating structures," *IEEE Trans. Plasma Sci.*, vol. 33, no. 4, pp. 1155–1160, Aug. 2005.

[14] C. Jing *et al.*, "Progress toward externally powered X-Band dielectric-loaded accelerating structures," *IEEE Trans. Plasma Sci.*, vol. 38, no. 6, pp. 1354–1360, Jun. 2010.

[15] C. Chang, J. Verboncoeur, S. Tantawi, and C. Jing, "The effects of magnetic field on single-surface resonant multipactor," *J. Appl. Phys.*, vol. 110, no. 6, Sep. 2011, Art. no. 063304.

[16] C. Jing *et al.*, "Observation of multipactor suppression in a dielectric-loaded accelerating structure using an applied axial magnetic field," *Appl. Phys. Lett.*, vol. 103, no. 21, Nov. 2013, Art. no. 213503.

[17] C. Jing, S. H. Gold, R. Fischer, and W. Gai, "Complete multipactor suppression in an X-band dielectric-loaded accelerating structure," *Appl. Phys. Lett.*, vol. 108, no. 19, May 2016, Art. no. 193501.

[18] M. C. Thompson *et al.*, "Breakdown limits on Gigavolt-per-meter electron-beam-driven wakefields in dielectric structures," *Phys. Rev. Lett.*, vol. 100, no. 21, May 2008, Art. no. 214801.

[19] C. Jing *et al.*, "Update on the development of externally powered dielectric-loaded accelerating structures," in *Proc. AIP Conf.*, vol. 1086, 2009, pp. 427–432.

[20] P. Zou, W. Gai, R. Konecny, X. Sun, T. Wong, and A. Kanareykin, "Construction and testing of an 11.4 GHz dielectric structure based traveling wave accelerator," *Rev. Sci. Instrum.*, vol. 71, no. 6, pp. 2301–2304, Jun. 2000.

[21] J. G. Power, W. Gai, C. Jing, R. Konecny, S. H. Gold, and A. K. Kinkead, "High power testing of ANL X-band dielectric-loaded accelerating structures," in *Proc. AIP Conf.*, vol. 647, 2002, pp. 156–164.

[22] W. Liu, "Design of dielectric accelerator using TE-TM mode converter," in *Proc. AIP Conf.*, vol. 647, 2002, pp. 469–475.

[23] W. Liu, C. Jing, W. Gai, R. Konecny, and J. G. Power, "New RF design for 11.4 GHz dielectric loaded accelerator," in *Proc. Part. Accel. Conf.*, Portland, OR, USA, May 2003, pp. 1810–1812.

[24] I. Syratchev, "Mode launcher as an alternative approach to the cavity-based RF coupler of periodic structures," CERN, Geneva, Switzerland, Tech. Rep. CERN-OPEN-2002-005, 2002.

[25] A. Kanareykin, "New advanced dielectric materials for accelerator applications," in *Proc. AIP Conf.*, vol. 1299, Nov. 2010, pp. 286–291.

[26] S. H. Gold *et al.*, "Development of X-band dielectric-loaded accelerating structures," in *Proc. AIP Conf.*, vol. 1299, 2010, pp. 292–296.

[27] J. Krupka, K. Derzakowski, B. Riddle, and J. Baker-Jarvis, "A dielectric resonator for measurements of complex permittivity of low loss dielectric materials as a function of temperature," *Meas. Sci. Technol.*, vol. 9, no. 10, pp. 1751–1756, Oct. 1999.

[28] Accessed: Jul. 2021. [Online]. Available: https://www.qwed.com.pl/resonators_te01.html

[29] HFSS. Accessed: Jul. 2021. [Online]. Available: https://www.ansys.com

[30] I. Wilson, "Surface heating of the CLIC main linac structure," CLIC-Note-52, CERN, Geneva, Switzerland, Tech. Rep., 1987.

[31] D. P. Pritzkau, "RF pulsed heating," Ph.D. dissertation, Dept. Appl. Phys., Stanford Univ., Standford, CA, USA, 2001.

[32] D. P. Pritzkau and R. H. Siemann, "Experimental study of RF pulsed heating on oxygen free electronic copper," *Phys. Rev. Special Topics Accel. Beams*, vol. 5, no. 11, Nov. 2002, Art. no. 112002.

[33] L. Laurent *et al.*, "Experimental study of RF pulsed heating," *Phys. Rev. Special Topics Accel. Beams*, vol. 14, no. 4, Apr. 2011, Art. no. 041001.

[34] P. B. Wilson, "RF-driver linear colliders," in *Proc. Part. Accel. Conf.*, Washington, DC, USA, May 1987, pp. 53–58.

[35] J. W. Wang *et al.*, "Accelerator structure R&D for linear colliders," in *Proc. Part. Accel. Conf.*, New York, NY, USA, Mar. 1999, pp. 3423–3425.

[36] A. Grudiev and W. Wuensch, "Design of the CLIC main linac accelerating structure for CLIC conceptual design report," in *Proceedings of the 25th Int. Linear Accel. Conf.*, Tsukuba, Japan, 2010, pp. 211–213.

[37] H. Zha and A. Grudiev, "Design and optimization of compact linear collider main linac accelerating structure," *Phys. Rev. A, Gen. Phys. Beams*, vol. 19, no. 11, Nov. 2016, Art. no. 111003.

[38] H. Zha and A. Grudiev, "Design of the compact linear collider main linac accelerating structure made from two halves," *Phys. Rev. A, Gen. Phys. Beams*, vol. 20, no. 4, Apr. 2017, Art. no. 042001.

[39] N. Catalan-Lasheras *et al.*, Experience operating an X-band high-power test stand at CERN," in *Proc. 5th Int. Part. Accel. Conf. (IPAC)*, Dresden, Germany, 2014, pp. 2288–2290.

[40] A. V. Edwards *et al.*, "Connection of 12 GHz high power RF from the XBOX1 high gradient test stand to the CLEAR electron linac," in *Proc. 10th Int. Part. Accel. Conf. (IPAC)*, Melbourne, VIC, Australia, 2019, pp. 2960–2963.

[41] Y. Wei, "A compact, low-field, broadband mode launcher for X-band DLA structures," in *Proc. AWA Needs Opportunities Workshop Argonne Nat. Lab.*, 2019, pp. 13–14. [Online]. Available: https://indico.fnal.gov/event/20265/contribution/25.

[42] H. Zha *et al.*, "Choke-mode damped structure design for the compact linear collider main linac," *Phys. Rev. Special Topics Accel. Beams*, vol. 15, no. 12, Dec. 2012. 122003

[43] A. Kanareykin, C. Jing, R. Kostin, and P. Avrakhov, "Dielectric based compact accelerator for industrial applications," in *Proc. 13th Workshop Breakdown Sci. High Gradient Accel. Technol. (HG)*, 2021, pp. 11–19. [Online]. Available: https://indico.fnal.gov/event/22025/contributions/210699/